THE JOURNAL OF PHYSICAL CHEMISTRY A

pubs.acs.org/JPCA Article

Pressure-Thresholded Response in Cylindrically Shocked Cyclotrimethylene Trinitramine (RDX)

Leora E. Dresselhaus-Cooper,* Dmitro J. Martynowych, Fan Zhang, Charlene Tsay, Jan Ilavsky, SuYin Grass Wang, Yu-Sheng Chen, and Keith A. Nelson

Cite This: *J. Phys. Chem. A* 2020, 124, 3301−3313 Read Online

ACCESS | Metrics & More | Article Recommendations | Supporting Information

ABSTRACT: We demonstrate a strongly thresholded response in cyclotrimethylene trinitramine (RDX) when it is cylindrically shocked using a novel waveguide geometry. Using ultrafast single-shot multi-frame imaging, we demonstrate that <100 μm diameter single crystals of RDX embedded in a polymer host deform along preferential planes for >100 ns after the shock first arrives in the crystal. We use in situ imaging and time-resolved photoemission to demonstrate that short-lived chemistry occurs with complex deformation pathways. Using scanning electron microscopy and ultra-small-angle X-ray scattering, we demonstrate that the shock-induced dynamics leave behind porous crystals, with pore shapes and sizes that change significantly with shock pressure. A threshold pressure of ∼12 GPa at the center of convergence separated the single-mode planar crystal deformations from the chemistry-coupled multi-plane dynamics at higher pressures. Our observations indicate preferential directions for deformation in our cylindrically shocked system, despite the applied stress along many different crystallographic planes.

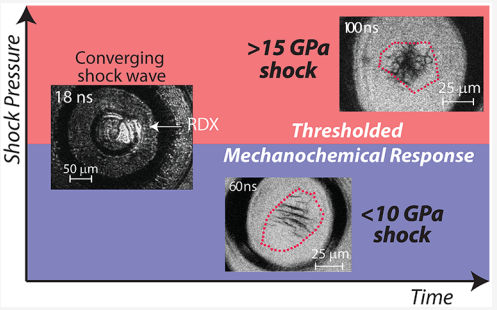

1. INTRODUCTION

Energetic materials are a class of reactive compounds that have decomposition pathways that can be activated by mechanical drivers.[1] Cyclotrimethylene trinitramine (RDX) is one such material, which has been used extensively for engineering, construction, and armament applications since it was developed in World War I.[2] In practical applications, RDX crystals are packed into a polymer binder to form polymer-bonded explosives (PBX) whose kinetics and detonation powers depend on their compositions. However, the mechanistic link between chemistry and mechanics has been elusive.[3] The hotspot model, first developed by Bowden and Yoffe, predicts that the chemistry in energetic materials initiates at locally high-temperature "hotspots."[4] Tarver, et al. found the critical conditions necessary for hotspots to reach self-sustaining levels (i.e., denotation) at the macroscale.[5] However, many uncertainties still exist about the microscopic mechanisms that activate critical or sub-critical hotspots.[6−12]

Early work on RDX demonstrated that explosives with more initial defects are more sensitive to shock-induced chemistry.[13,14] Ductile[15,16] and brittle[17,18] responses in RDX have been predicted and observed under different conditions. Different chemical mechanisms have been observed for decomposition activated by different strain rates.[19−21] Shock waves produce the highest attainable strain rates to mechanically driven systems, and the extreme pressure-temperature states that they create can induce exotic chemistry that is not accessible at ambient conditions.[22] Since shock waves irreversibly destroy materials through pathways that are extremely sensitive to variation among samples down to the nanoscale, shock responses of materials are notoriously difficult to characterize.[23] Detailed measurements of shock-induced reactive pathways have been limited, despite the practical needs for the scientific insight that such measurements could provide.

Molecular dynamics studies by Cawkwell et al. have demonstrated that shocks in RDX along the ⟨001⟩ axis form shear bands, as their slip systems cannot accommodate the strain.[15,24] Theoretical work by other groups has also indicated pressure-dependent anisotropic plasticity in uniaxially shocked RDX.[25−28] Near-equilibrium indentation tests have probed the active deformation planes in RDX, revealing 14 active planes in the *Pbca* crystal (a = 13.182 Å, b = 11.574 Å, c = 10.709 Å),[29] with localized plasticity and fracture around the indentation tip.[16,30−32] At large length scales, fracto-emission has been observed as detonations are initiated in RDX,[17] while shocked, small RDX crystals have shown additional slip, cleavage, and shear bands after shock loading.[33,34] Several different chemical decomposition mechanisms are known to compete, and

Received: August 10, 2019
Revised: January 31, 2020
Published: February 1, 2020

https://dx.doi.org/10.1021/acs.jpca.9b07637
J. Phys. Chem. A 2020, 124, 3301−3313

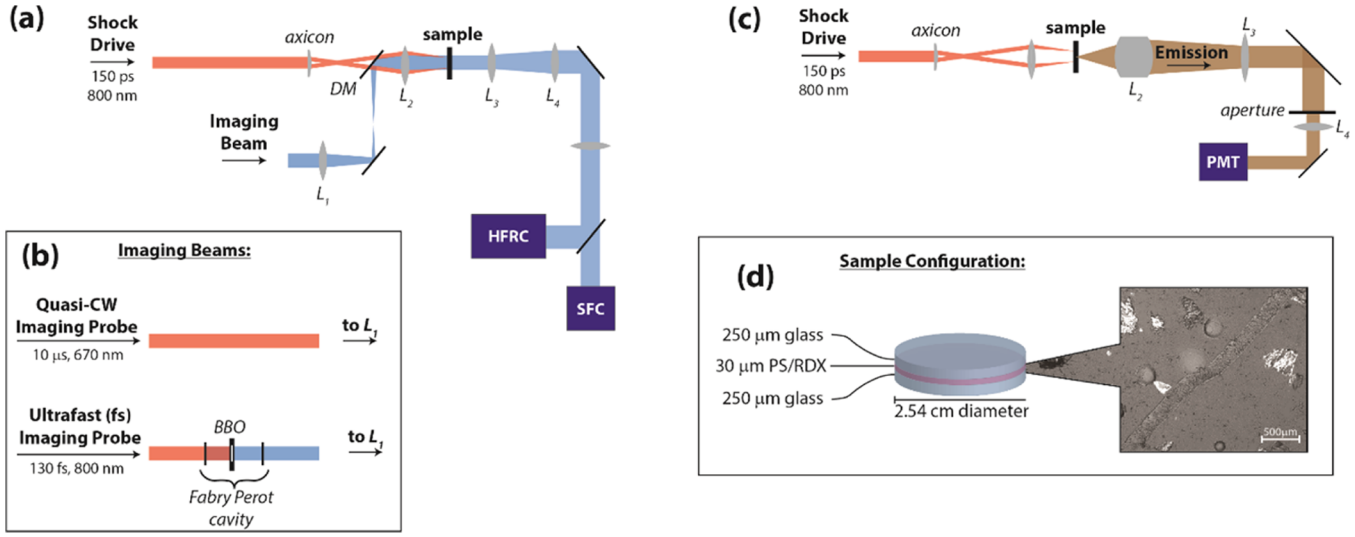

Figure 1. (a) Schematic illustration of the shock and imaging configurations used to collect real-time images with a high-frame-rate camera (HFRC), and the "before" and "after" frames on a single-frame camera (SFC); (b) schematic illustrations of the uncollimated quasi-CW and femtosecond imaging beams before reaching lens L1. (c) Optical configuration used to measure shock-induced emission. (d) The sample geometry, with an image of part of a typical sample.

predictions have shown different relative extents based on the shock pressure.[35,36] While chemistry and plastic transformations have always been predicted and observed to occur together, a direct link between the detailed modes of deformation and the chemical pathways has remained elusive.

Our view of the dynamics induced by idealized uniaxial shocks is still incomplete, but real-world PBXs experience more complex, highly non-planar shock geometries. The heterogeneity in a PBX creates many interfaces, resulting in multiple reflections and refractions that distort the planarity of an initially planar shock wave.[11] While experiments on simple materials have explored how the geometry of a shock wave influences the material dynamics that ensue,[37,38] the effects of non-planar shocks on energetic materials remain largely unknown. Work by An et al.[11,39] has modeled how heterogeneities in PBX materials cause an initially planar shock to deform into non-planar waves, which initiate hotspots to different extents than the planar waves. To understand how RDX decomposes in PBXs and to inform the design of mechanically driven chemical systems, detailed experimental studies must be extended to non-planar shock waves.

This work examines how cylindrically converging shock waves initiate deformations and chemistry in RDX. We use a novel quasi-2D waveguide shock geometry that enables us to observe how RDX crystals that are immobilized in a polystyrene matrix respond to cylindrical shocks. With single-shot multi-frame image sequences, we track the progression of the deformations induced by converging shock waves. We see a high degree of crystallographic alignment in the deformations, despite the many directions along which the shock stresses are exerted. Scanning electron microscopy (SEM) and ultra-small-angle X-ray scattering (USAXS) demonstrate that the crystals recovered after they are shocked have pore structures with sizes and morphologies that depend strongly on the shock pressure. Real-time imaging and photoemission results indicate a strong pressure threshold in the shock-induced chemistry and deformation. Above a ~12 GPa pressure threshold, we observe a cascade of deformation planes that appear and shift for >20 ns after the shock has passed and that are correlated with increased chemical decomposition. Our in situ imaging and fluorescence results as well as our ex situ X-ray scattering results provide new insights into the links between mechanical deformation and chemistry in shocked RDX.

2. EXPERIMENTAL METHODS

2.1. Shock Experimentation and Sample Preparation.

All waveguide shocks in this work were produced by pulsed laser excitation (150 ps, 1−9 mJ, 800 nm) with a Gaussian drive laser beam that was passed through a 0.5° axicon and an f = 30 mm lens to form a ring-shaped drive with 150 μm diameter at the sample.[40] An absorbing laser dye (Epolin 30361[a]) dissolved in the polystyrene sample absorbed the drive laser light, initiating thermal expansion that launched the compressive wave. Real-time images of the shock-induced dynamics were collected with single-shot multi-frame imaging, with femtosecond or nanosecond integration times to probe different timescales (Figure 1a). For femtosecond multi-frame imaging (Figure 1b, bottom), the compressed 800 nm, 130 fs laser output was passed through a frequency-doubling Fabry−Perot cavity to create a train of 400 nm femtosecond imaging probe pulses, spaced 3−5 ns apart in time.[41] Nanosecond multi-frame image sequences (Figure 1b, top) were collected with a 10 μs duration, 670 nm wavelength SILUX diode laser as the light source, using the camera to electronically gate the pulse. Both imaging configurations (Figure 1a) included an ultra-high-frame-rate SIM 16× camera to collect the image sequences in real time. A single-frame Hamamatsu Orca camera was used to align the crystals and image the recovered samples.

Shock-induced emission from the substrates, the polymer, and the RDX were measured in a similar configuration, as shown in Figure 1c. The imaging probe beam was blocked, and the light emitted from the sample was imaged with a 10× objective and a subsequent f = 1000 mm lens followed by an aperture. The aperture spatially filtered the emitted light, allowing us to remove most of the laser-induced fluorescence from the excitation "ring" region (some persisted, due to scatter at the aperture). Light passing through the aperture was

https://dx.doi.org/10.1021/acs.jpca.9b07637
J. Phys. Chem. A 2020, 124, 3301−3313

Table 1. Predicted Shock Velocities and Pressures, Assuming Transduction at R_s = 20 μm, Shocked States Using the Principal Hugoniot, and the CCW Model for Acceleration

drive laser energy [mJ]	U_s in polystyrene at interface with RDX (measured by LADA) [km/s]	U_s in RDX at interface (R_s = 20 μm) [km/s]	interface pressure of RDX on principal Hugoniot [GPa]	U_s in RDX at R_s = 5 μm (10% unc. in U_s before CCW) [km/s]	pressure at R_s = 5 μm on principal Hugoniot (10% unc. in U_s before CCW) [GPa]
1.5	1.6	3.09 ± 0.02	0.92 ± 0.085	4.5 ± 0.2	7 ± 3
2.5	2.0	3.41 ± 0.04	2.0 ± 0.15	4.9 ± 0.3	10 ± 3
3.5	2.3	3.67 ± 0.04	3.1 ± 0.2	5.7 ± 0.3	16 ± 5
4.5	2.5	3.8 ± 0.25	3.9 ± 0.7	7.0 ± 0.4	28 ± 7

imaged with an f = 100 mm lens onto a photomultiplier tube, and the resulting signal was collected and saved on a 4 GHz bandwidth oscilloscope. For each drive pulse energy, emission profiles were measured from the shocked polymer with and without an RDX crystal inside the shock ring, with repeated measurements at each drive pulse energy to reveal reproducible features of the responses.

Samples were made by embedding a collection of small (25−300 μm dimensions) RDX crystals into a matrix of polystyrene with a dissolved 800 nm absorptive laser dye (Epolin 3036). The small crystals were grown under ambient conditions by slow evaporation from a solvent mixture made by adding dimethylformamide (18% vol) to a saturated solution of RDX in acetonitrile. The resulting crystals were suspended in a solution of polystyrene (15% mass) and Epolin 3036 (1% mass) in toluene (84% mass) and were drop-cast onto 2.54 cm diameter fused silica microscope slides (250 μm thick). Polystyrene was chosen for the polymer matrix because it had good adhesion to the RDX crystals, and its acoustic impedance nearly matched that of RDX. After drying for 48 h, the sample layer was polished to ∼50 μm thickness using aluminum oxide lapping paper in a water−alconox solution with a minimum grit size of 500 nm. Samples with the "capped" geometry were made by placing a thin layer of glycerol over the polished film (the capping fluid) and another 250 μm thick fused silica slide to seal the sample. Samples of the "uncapped" geometry were made by rewetting the polished film with a thin layer of toluene and pressing the second fused silica substrate atop the damp sample layer to create a tight seal. After they were sealed, the uncapped samples were fitted inside a compressive clamp and dried under vacuum for 12 h. While the capped samples had an accessible surface for some ex situ characterization methods that required removal of the top substrate, the low impedance of the capping fluid reduced the confinement of the shocks. Uncapped samples had good surface contact between the sample and both substrates, providing high optical quality and shock confinement in the waveguide geometry. The thickness of each uncapped sample was measured with a Keyence CK-X200 confocal microscope. Specific sample thicknesses and shock pressures were 37.5 μm (7 GPa), 28 μm (10 GPa), 34 μm (16 GPa), and 33 μm (28 GPa).

RDX crystals in the polystyrene matrix had slight mobility as they were polished, which created poor surface quality in crystals that were located at the polished surface of the sample layer. To ensure that our measured RDX responses were not influenced by mechanical perturbation and crystal surface damage during polishing, we limited all experiments (except for SEM measurements) to embedded crystals that were never in direct contact with the lapping paper. A single sample assembly typically contained 50−500 RDX crystals that were suitable for shock measurements.

The highly heterogeneous samples were placed in the "sample" position in the optical configurations shown in Figure 1 and were then translated using a three-dimensional sample stage. We used the single-frame camera to locate RDX crystals with ≤125 μm diameter and to position them to receive a converging shock launched in the surrounding polymer. We then used a shutter and a set of Stanford Research Systems DG535 timing boxes to synchronize our drive beam and multiframe camera, and we collected image sequences of the shock traveling through the polymer and the RDX crystal as well as subsequent shock-induced responses.

2.2. Determination of Pressure. The shocks within the RDX crystals did not produce discernible imaging signals in the uncapped geometry (likely due to small photoelastic constants, as described in the Results section). However, we could monitor shock propagation in the polymer matrix before the shock entered a crystal, and from the shock velocity in the polymer, we could estimate the shock velocity (U_s) and pressure (P) states reached in the RDX crystals in uncapped samples. We used a boundary-detection image-processing algorithm called locally adaptive discriminant analysis (LADA)[42,43] to locate the shock in each frame while it was still in the polymer. Knowing the time between frames, we could determine the average velocity of the shock wave, U_s, as it converged toward an RDX crystal. The impedance-matching method allowed us to convert the measured polymer U_s value to a corresponding RDX U_s value at the interface, assuming that the shocked states lie along the principal Hugoniot of each material.[44] We used the literature parameters for the shock Hugoniot of RDX, but adjusted the acoustic velocity of polystyrene to the C_0 = 1.1 km/s value that we measured for the waveguide system.

Using the calculated U_s value in RDX at the interface as the initial condition, we used the Chester−Chisnell−Whitham (CCW) model[45−47] of the accelerating shock to calculate the U_s values in RDX at all times as the shock converged.[47] While the model yields shock velocity values that do not necessarily lie along the principal Hugoniot, we used the Hugoniot to relate our predicted shock velocities to the corresponding shock pressures at the shock front. Our previous work[41] showed that the converging geometry and edge effects from partial confinement in the waveguide structure cause the actual shock pressure to deviate by 2−10% from the Hugoniot as the shock approaches the center of convergence for 30 μm thick waveguides.[41] We also estimated a shock focal spot size of 5 μm diameter. This value is based on previous studies that demonstrated that our converging waveguide shocks deviate substantially from the principal Hugoniot for R_s < 5 μm.[41] A strong deviation from the Hugoniot is inevitable in a focusing shock, as the pressure is highest at the focus but the net particle velocity is zero. The estimated values for the shock parameters resulting from different shock drive laser pulse

https://dx.doi.org/10.1021/acs.jpca.9b07637
J. Phys. Chem. A 2020, 124, 3301−3313

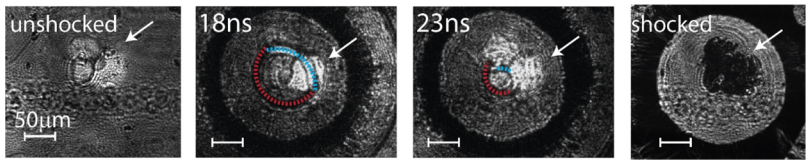

Figure 2. Direct shadowgraph images showing a shock wave produced by drive laser pulse energy, E_{drive} = 3.5 mJ, in a capped sample as it traverses an RDX crystal. The crystal is indicated by the white arrow; the shock in polystyrene is shown with red dashed lines, and the shock in RDX is shown with blue dashed lines. The images were collected using femtosecond-duration probe pulses (as shown in the lower part of Figure 1b) to resolve the propagating shock wave without blurring. Images were collected without crossed polarizers.

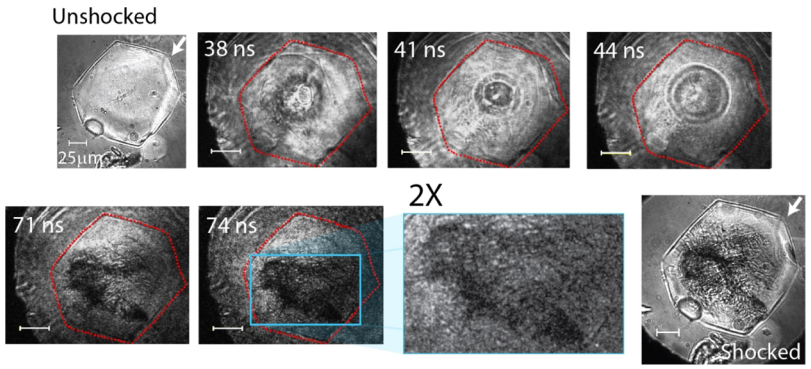

Figure 3. Direct shadowgraph images of an ∼7 GPa shock produced by E_{drive} = 2.0 mJ traversing a crystal of RDX in the uncapped sample geometry. The white arrow in each frame indicates the RDX crystal, which is outlined in red. An expanded (2×) and brightened view is shown of the damaged region of the crystal in the frame at t = 74 ns. Images were collected without crossed polarizers.

energies, and the uncertainties in the shock parameters, are shown in Table 1. Some reassurance that the uncertainties are not greater than those indicated in the table comes from the fact that as presented below, we observed different pressure-dependent responses repeatedly for different RDX crystals, depending with high consistency on the drive laser pulse energies. We also observed similar responses extending across significant regions of shocked crystals, clearly indicating that there is not an extremely sharp focus in one region at which the pressure is highest. Altogether, we conducted observations on 5−10 different RDX crystals for each of the four drive pulse energies listed below.

3. RESULTS

3.1. Ultrashort-Window Images of Shock Propagation and Response. The morphology and velocity of the converging shock in the RDX crystals were most clearly observable in image sequences of capped samples, as shown in Figure 2. The blue and red lines at 18 and 23 ns show the angular components of the converging shock ring that traverse the RDX crystal and polystyrene, respectively (see the Supporting Information for additional details). A comparison between the red and blue lines in Figure 2 reveals that the shock velocity is higher for the components that traverse the stiffer RDX crystal than the surrounding polymer. As the crystal is non-cylindrical, the shape of the shock ring changes as it traverses the RDX, with leading angular components corresponding to the components of the shock that have traversed the longest distance in the crystal. The change in the curvature and velocity of the shock wave verifies that the shock wave transmits (at least in part) into the RDX crystals.

The unambiguous change in velocity and curvature in Figure 2 are observable only in capped samples, as the shock in RDX is coupled to the capping fluid, whose high photoelastic constant produces a clear feature in the image. The capping fluid reduces the degree of confinement of the shock within the RDX sample layer, modifying the material dynamics. While the capped samples were necessary to directly validate that the shock transmits into RDX crystals, the uncapped samples were required for a better constrained $P-U_s$ relationship (section IV, Supporting Information). All of our analysis of shock-induced RDX responses comes from uncapped samples.

An image sequence of a similar converging shock traversing an RDX crystal in the uncapped geometry is shown in Figure 3, revealing the material dynamics following the shock. The shock wave is evident in frames collected at t = 38, 41, and 44 ns as a set of concentric rings inside the laser excitation ring. At t = 38 ns, the wave is converging, with the shock front corresponding to the innermost ring. The contrast in the direct shadowgraph images is described by the Laplacian of the sample's refractive index, showing a shock as a bright and then dark intensity feature that scales with the density variation, $\partial^2\rho/\partial r^2$, at the shock front and release, respectively. As the shock front appears as the bright leading edge of the shock feature, it is evident in Figure 3 that the wave is diverging at t = 41 and 44 ns.

A close examination of the initial three frames in Figure 3 shows that the RDX crystal in these frames contains a large population of poorly resolved, somewhat indiscernible shapes. Indistinct image features like those seen in Figure 3 can correspond either to objects that are significantly out of the focal plane of the imaging system or to objects that are slightly smaller than the resolution of the imaging configuration. Further imaging of the recovered crystal with confocal scanning in a diffraction-limited microscope (magnification ≤ 100×) demonstrated that these features cannot be resolved for any focal plane in the sample. Given the 0.28 numerical aperture (NA) for the in situ imaging configuration in Figure 3, the diffraction limit with our 400 nm illumination was $\lambda/(2NA)$ = 710 nm, placing an upper bound on the size of the

https://dx.doi.org/10.1021/acs.jpca.9b07637
J. Phys. Chem. A 2020, 124, 3301−3313

features. As is evident at 38 and 41 ns, the sub-micrometer features appear radially at a distance of ~4 μm after the leading edge of the shock front. By dividing the radial distance between the shock front and the initial RDX response by the average shock velocity (~4 km/s), we see that the sub-micrometer features appear within the first 1 ns of the shock front. Given the ~15−20 ns duration of the elevated pressure in the waveguide converging shocks,[48] the results in Figure 3 indicate that sub-micrometer features appear before the material returns to ambient pressure.

3.2. Analysis of Crystals Recovered after Shock. To investigate the shock-induced nanoscale features produced in the RDX, we used SEM and USAXS on recovered crystals. Together, these two measurements reveal much about the morphologies and the statistics of void structures that are formed by the shock waves.

SEM analysis was conducted on shocked crystals in capped samples because these had accessible polished crystal faces at the sample surfaces. Crystal motion in the polymer host as the samples were polished worsened the surface smoothness, but representative populations of shocked and unshocked RDX crystals revealed distinct differences in their SEM images. A representative unshocked crystal can be seen in Figure 4a, while a representative crystal recovered after shock is shown in Figure 4b.

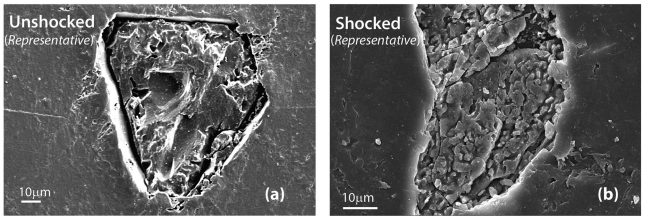

Figure 4. SEM images of two representative RDX crystals, (a) one before and (b) the other after shocking. The recovered crystal clearly indicates the porous structure seen after shocking. The drive laser pulse energy was 3.5 mJ for an RDX crystal embedded in a capped sample.

Crystal facets are evident in the unshocked crystal in Figure 4a, indicating its single crystallinity (as confirmed by X-ray diffraction). The morphology of the shocked crystal in Figure 4b indicates an intricate network of cracks and voids covering length scales from micrometers to nanometers. Similar porous structures have been observed in RDX crystals upon slow thermal decomposition[49] because localized chemical decomposition left voids. In our experiment, the shock waves may cause similar localized chemical decomposition to create nanoscale voids. Yoffe and Bowden predicted that trapped bubbles of gaseous products could destabilize energetic crystals as their chemistry is activated.[4] A qualitative view of Figure 4b suggests that the voids are ~1 μm in size, but because SEM probes only the material's surface, the image could not be used to quantify the statistics of the void structures. We were unable to zoom into the crystals with a higher resolution than that shown in Figure 4 by SEM, as the focused electron beam decomposed the crystals.

We used USAXS to measure the sub-micrometer void structures in the uncapped sample geometry and to obtain statistically significant, quantitative data about the void structures. USAXS data were acquired using the USAXS instrument at the Advanced Photon Source, Argonne National Laboratory.[50] We measured a representative population of pristine RDX crystals and recovered crystals that had been shocked to maximum pressures of 10, 16, and 28 GPa. USAXS measures the scattering intensities produced due to differences (contrast) in electron density. In the case of RDX, after shock, the void structure has very low electron density from any product gases. Hence, shocked crystals produced additional scattering signals that originated from the distribution of void sizes inside each crystal (as compared to USAXS from unshocked RDX). We measured the approximate average size, morphology, and volume fraction of the voids by modeling the scattering profiles. We used the information from SEM images for initial fitting parameters (i.e., the mean size, minimum size, volume fraction, and aspect ratio) to model the USAXS data.

Figure 5 shows USAXS profiles of RDX crystals after they were shocked to P = 10, 16, and 28 GPa as well as an unshocked RDX crystal, all in the uncapped sample geometry. The increase in the scattering intensities of the shocked samples, when compared with that of the unshocked sample, can be attributed to an increase in scattering from void structures like those observed in Figure 4. USAXS data reduction and analysis for the shocked RDX samples were conducted using the SAS analysis package in Indra and Irena, respectively.[51] An example of the model is shown in the inset of Figure 5. The total scattering intensity is modeled as the sum of a scattering baseline and void scattering. More discussion about this type of scattering model can be found elsewhere.[52] The scattering baseline is constructed based on the scattering signal when the shock-induced voids are not present, that is, from the unshocked crystal. The void scattering is described by a population of spheroids spatially separated according to the dilute limit. The modeling results are summarized in Table 2.

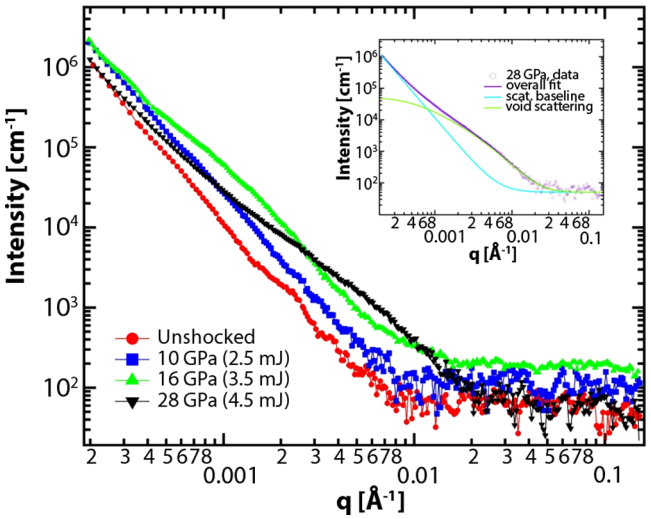

Figure 5. USAXS profiles acquired from an unshocked RDX crystal and from representative crystals recovered after being shocked to pressures P = 10, 16, and 28 GPa in the uncapped sample geometry. All profiles shown here have been corrected for sample thickness and background scattering to provide the absolute scattering intensities. Inset shows scattering and fit from 28 GPa shocked crystal.

As shown in Table 2, the results from the USAXS data indicate changes in the average size, number density, and morphology of voids with increasing shock pressure. For

https://dx.doi.org/10.1021/acs.jpca.9b07637
J. Phys. Chem. A 2020, 124, 3301−3313

Table 2. Void Distributions from Shocked RDX Samples[a]

P [GPa]	mean R_g [nm]	spheroid aspect ratio	volume fraction	number density
10	497 ± 8	6.1	0.0064 ± 0.0005	$(1.8 \pm 0.2) \times 10^{9}$
16	193 ± 12	2.1	0.0085 ± 0.0003	$(1.4 \pm 0.1) \times 10^{11}$
28	30.8 ± 12	1.3	0.0071 ± 0.0002	$(2.8 \pm 1.0) \times 10^{13}$

[a]In all cases, the scattering profiles were calculated after background subtraction of the baseline scattering contribution, using the calculated scattering cross section of $\sigma = 245.5 \times 10^{20}$ cm^{-4} and an RDX mass density of 1.799 g/cm^3.

increasing shock pressure, the average void size decreases significantly, while the aspect ratio shifts from an oblong geometry at low shock pressures to a nearly spherical shape by P = 28 GPa. The pressure-dependent changes in void morphology, not directly measured previously, suggest that increased shock pressure may activate new mechanisms to form voids. The dramatic increase in the number density of voids with increasing shock pressure (100-fold increase for each increment) also suggests a pressure-dependent change in the mechanism that causes the voids to form.

3.3. Time-Dependent Emission from Shocked Samples. To investigate the dynamic origins of the shock pressure-dependent responses in the RDX crystals, we measured the time-resolved shock-induced emission from them. The traces displayed in Figure 6 show the time-dependent intensity of photoemission produced by shocked samples of RDX (red) as compared to the polymer background (blue) at each shock pressure. We note that any additional emission from adiabatic heating in trapped air and fluorescence from the glass and laser dyes are all included in the polymer background traces. All traces in Figure 6 show significant photoemission from the polymer layer initially and do not show significant photoemission beyond t = 50 ns. Comparing the RDX and polymer emission traces indicates a clear threshold pressure of $P \approx 12$ GPa for RDX emission to occur. While low-pressure shocks produced no RDX emission that was discernible above the background signal, high-pressure shocks generated additional emission from the RDX crystals for <50 ns. Images of the unshocked and recovered crystals showed that all crystals shocked to $P > 8$ GPa showed discernible damage upon recovery. Combining these results demonstrates that damage generated below $P \approx 12$ GPa was linked to short-time photoemission, suggesting a change in the mechanism of damage in that pressure range.

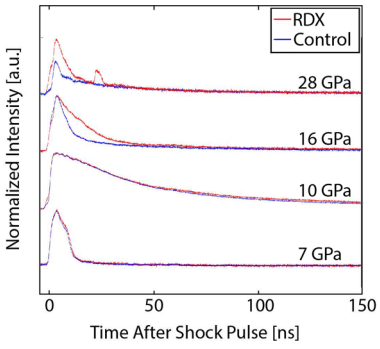

Figure 6. Photoemission traces produced by uncapped samples in response to shock waves in our waveguide geometry at four different drive laser pulse energies. Blue traces correspond to representative control emission traces that include the background emission produced by the immobilizing polymer and glass substrates without an RDX crystal, while red traces include the RDX crystal. The extra emission peak in the 28 GPa trace is an artifact generated by reflection of stray light from elsewhere in the optical system. The peak emission amplitudes at different pressures are normalized to the same height and do not indicate the relative intensities of signals from one pressure to the next. The amplitudes of emission from samples with and without RDX were normalized to the same levels at long times.

3.4. Images of Deformation. An RDX crystal shocked to a pressure of 10 GPa at the focus is shown in the image sequence in Figure 7. Parallel deformation planes appear early as striking features and persist throughout the subsequent images; the number of discrete deformation planes and the strength of the depolarization that they produce evolve over the image sequence. The directions, lengths, and propagation of the parallel deformations shown in Figure 7 are characteristic of the trends we observed for moderate-pressure shocks. As determined by single-crystal X-ray diffraction, this crystal was oriented such that the imaging light propagates normal to the $(\bar{2}10)$ plane. With the 5 ns integration time, the images were unable to resolve the shock wave. The uncollimated imaging light from the diode laser provided high sensitivity to the depolarization induced by the crystal deformations.

While the shock wave is not visible with the 5 ns integration time, femtosecond-image sequences recorded under similar conditions indicate that the shock reached the center of convergence at $t \approx 28$ ns. The shock timing indicates that deformations in the crystals began to form within 5 ns of the shock's arrival. For the first 30 ns shown in Figure 7 (t < 60 ns), the initial deformation lines appear, elongate, and create new lines all along the same direction. The deformation lines initially grow darker with time, reaching their fullest extent around t = 65 ns, and then fade somewhat. Features resembling those in Figure 7 were never observed in samples with only polystyrene and no RDX present. Neither glass nor polystyrene has long-range order that would introduce reproducibly preferential deformation planes at 5−50 μm length scales during or after the shock.[53,54] It is clear that the reproducibly parallel features in the images originate from the shocked RDX.

The intensity variation that indicates the growth of the deformation lines is easier to observe with pseudo-color, as shown in Figure 8a. The linear feature positions and shapes found by the LADA image recognition software[42,43] correspond to the maps shown in Figure 8b, providing a clear view of the growth and coalescence of the deformation features.

Figure 8 demonstrates that the linear deformation planes grow significantly between each 5 ns frame. While each line is quite short at t = 30 ns, the lines circled in red grow slightly and coalesce over the first few frames. Similar coalescing features may be seen for other lines across the entire sequence, suggesting that crystallographic planes may have originally been destabilized in multiple places, at smaller length scales than our ~1 μm resolution. At t = 60 ns, the bottom pair of deformation lines appears to link along a new direction that is nearly perpendicular to the primary deformation direction.

The deformation map in Figure 8 demonstrates the characteristic behavior observed in systems with P < 12 GPa,

https://dx.doi.org/10.1021/acs.jpca.9b07637
J. Phys. Chem. A 2020, 124, 3301−3313

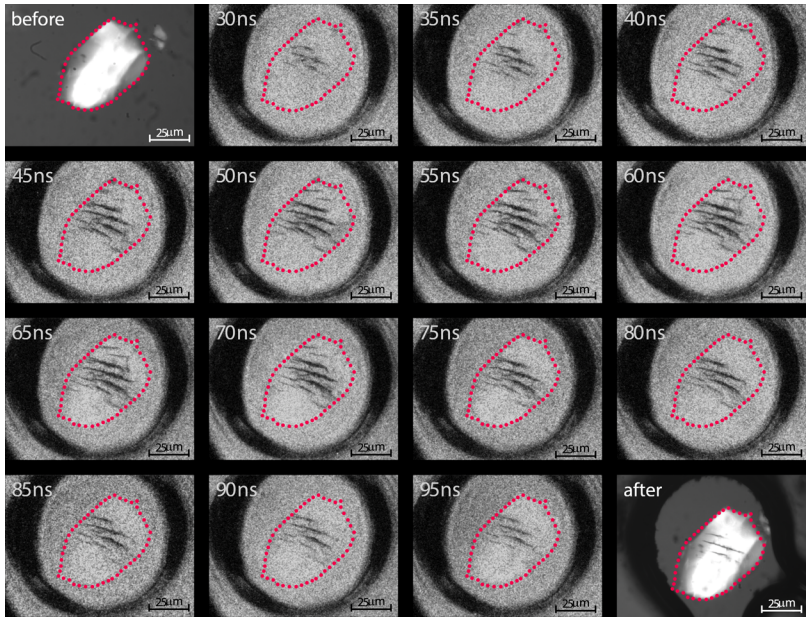

Figure 7. Image sequence showing the onset and growth of deformation planes produced by a shock of $P \approx 10$ GPa using $E_{drive} = 2.8$ mJ. The sequence was collected with the uncollimated quasi-CW imaging light, with a 5 ns integration time for each frame. All images were collected through crossed polarizers. The dotted line indicates the outline of the shocked RDX crystal.

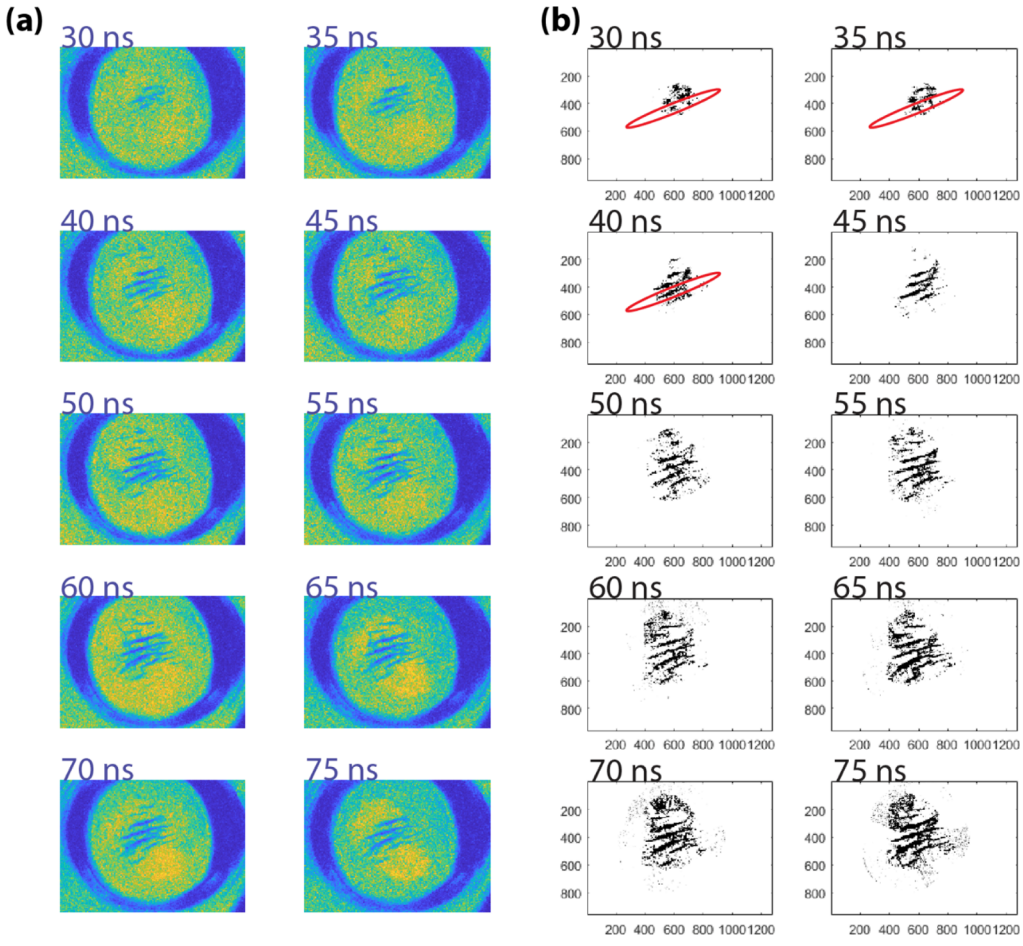

Figure 8. (a) Portion of the image sequence displayed in Figure 7 showing the growth of parallel-line features, with pseudo-color to show the intensity variation. These dark features were then located with the LADA image recognition algorithm,[42,43] providing a map of the discrete lines from each frame (b). The red ellipses in the first three frames of (b) show the growth of a single deformation plane.

https://dx.doi.org/10.1021/acs.jpca.9b07637
J. Phys. Chem. A 2020, 124, 3301−3313

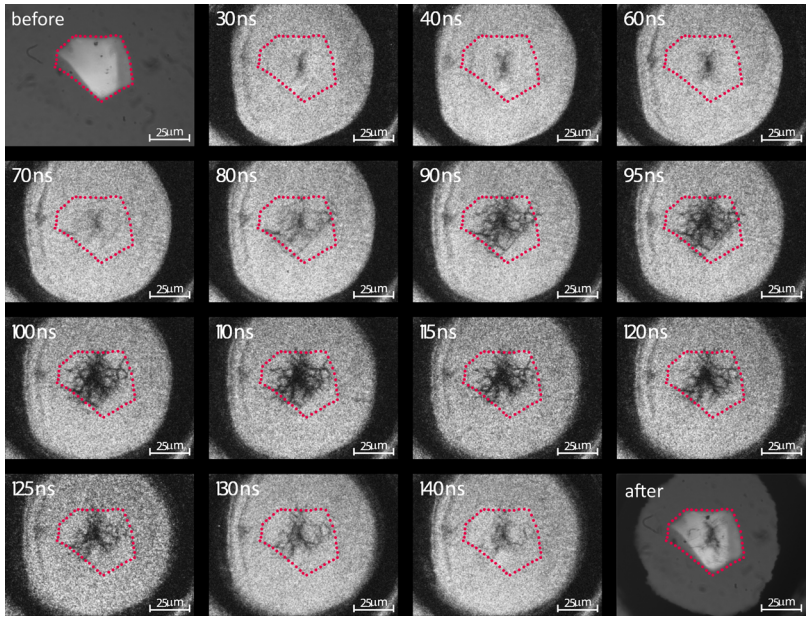

Figure 9. Image sequence for an RDX crystal (outlined in red) shocked with a pressure that reaches 28 GPa at the center of convergence (produced by a 4.5 mJ drive laser pulse). The image sequence was collected through crossed polarizers with a 5 ns integration time.

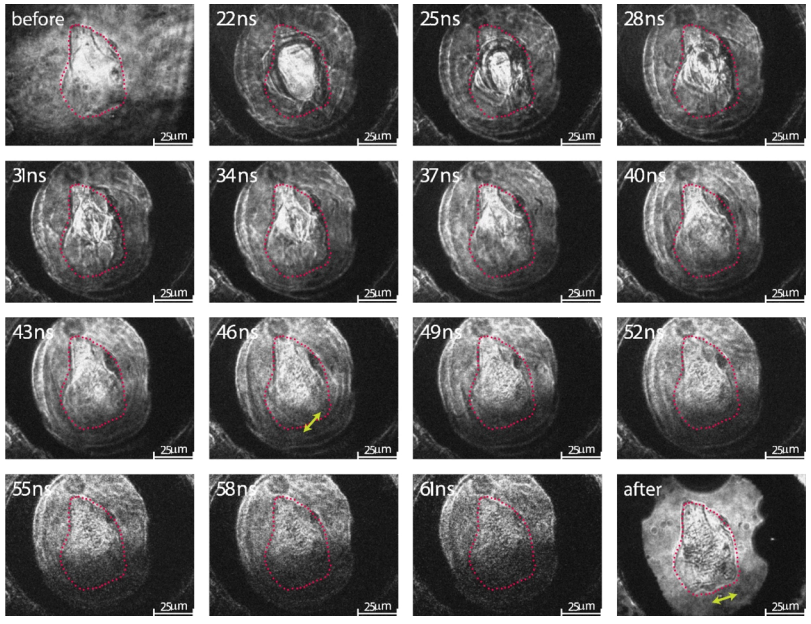

Figure 10. RDX crystal outlined in red is shocked to $P \approx 28$ GPa (with $E_{drive} = 4.5$ mJ) and monitored using femtosecond multi-frame imaging. The yellow arrows in frames at 46 ns and after show two deformation directions. Collected without crossed polarizers.

which may be seen in other image sequences in the Supporting Information. Crystals shocked with $P > 12$ GPa, however, produced different deformation dynamics.

The images in Figure 9 demonstrate the typical trends for the growth, propagation, and fading of deformation features following the converging shock that reaches considerably higher pressure (~28 GPa) in RDX. While the darkest deformation feature is located at the center of convergence, additional deformation planes span much of the crystal in multiple directions. The image sequence in Figure 9 illustrates that converging shocks reaching a pressure considerably higher than 12 GPa induce deformations that are much more extensive than in the low-pressure case. We were unable to map the characteristic directions of the high-pressure deformation planes from Figure 9 because the crossed polarizers' thresholded high sensitivity produced shadows from all portions of each overlapping deformation lines, blurring our view of each specific line.

To resolve the complicated deformation pathways occurring for shocks of $P > 12$ GPa, femtosecond-resolution image sequences were taken over a 48 ns interval. The 16-frame sequence in Figure 10 demonstrates the high-pressure deformation progression as resolved by femtosecond shadowgraph imaging. No polarization gating was used. The shadowgraph images clearly resolve the deformation pathways with large spatial variations in $\nabla^2 n$ (n is the refractive index) to resolve the evolution of deformation planes for high-pressure shocks.

https://dx.doi.org/10.1021/acs.jpca.9b07637
J. Phys. Chem. A 2020, 124, 3301−3313

Frames at t = 22 ns through t = 28 ns in Figure 10 contain the dark rings corresponding to the converging shock in the polymer. From t = 28 ns to t = 34 ns, the shock gives rise to complicated image features arising from partial reflections that occur each time the shock reaches the polymer−crystal interfaces.[55] Over this time, the shock converges to a focus and subsequently diverges. By t = 37 ns, the shock pressure is too low to produce visible features in the images. All new image features that appear from t = 37 ns through the end of the experiment (as well as some of the earlier features) reveal dynamics occurring in the RDX crystal as the material responds to the shock.

Like the images in Figure 3, the crystal in Figure 10 reveals indistinct linear features that appear from t = 40 ns to t = 43 ns and that show a clear directional preference parallel to the yellow arrow in the frame at t = 46 ns. These indistinct features that appear ∼14 ns after the shock entered the RDX crystal originate from either increased scattering or changes to the refractive index. Changes to the refractive index could indicate either additional compression or phase transitions along these lines, while enhanced scatter at the features would indicate a collection of localized sub-micrometer void structures, similar to those observed in Figure 3. In this case, given that these features appear and evolve upon release and recovery from the shock pressure, we hypothesize that these features may indicate either nanofractures or accumulating defect pile-ups with <1 μm sizes.[56] As RDX has shown both brittle and ductile responses, the character of these indistinct features is unclear and further experiments are required to identify the cause of the lines. By t = 46 ns, the initially poorly resolved shapes develop into discernible (though diffuse) lines along the same direction that was indicated initially. Similar diffuse linear features following the shock wave were evident only in limited cases (shown in the Supporting Information), as they depended strongly on the shock pressure and crystal orientation.

From t = 46 ns until the end of the experiment, discernible lines appear in the crystal that correspond to deformations along specific directions, the primary seven of which are annotated in Figure 11. We reference the observed angles between each plane to the first plane to appear, highlighted in blue and labeled as 0°. In the first frame in Figure 11, we observe four families of deformation planes along 0°, 11°, 59°, and 66°, with an additional family of planes appearing 3 ns later along −24° and another 3 ns later along 108°. The recovered crystal shows an additional seventh family of deformation planes along 130°, which appeared after the 48 ns window of the experiment.

We do not provide a detailed account of the evolution of the linear features, as their diffuse structure makes quantification rather subjective. However, the annotated and unannotated frames in Figure 11 demonstrate that both the lengths and number densities of the planes along different directions show different kinetics and different extents of deformation. While the growth kinetics differ between planes, each direction of planes generally appeared as a series of short lines that shifted within the crystal and ultimately coalesced into the final longer deformations.

A close look reveals both evolution and apparent motion of some linear features over the progression of images. Figure 12 displays a further enlarged view of the same RDX crystal, with consistent locations annotated with dashed lines to clarify the changes and motion.

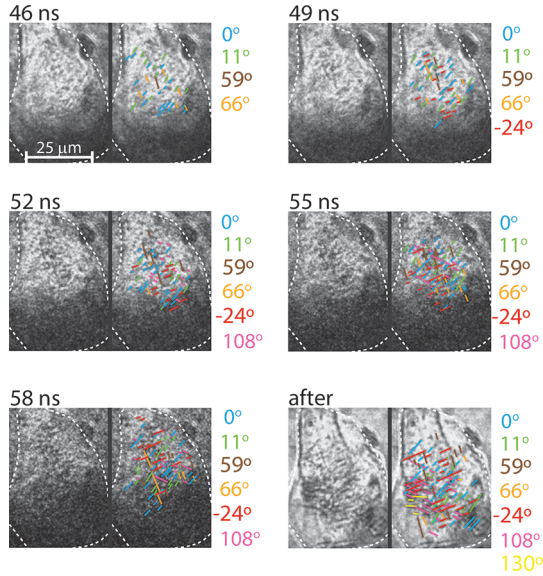

Figure 11. Enlarged images from Figure 10 showing the deformation pathways during a 12 ns interval. Each image is shown annotated (right) and unannotated (left) for each frame. Annotations show the direction of each family of deformation plane with lines of a different color, as labeled on the right. All planes are referenced to the first plane to appear, whose direction we define as 0°.

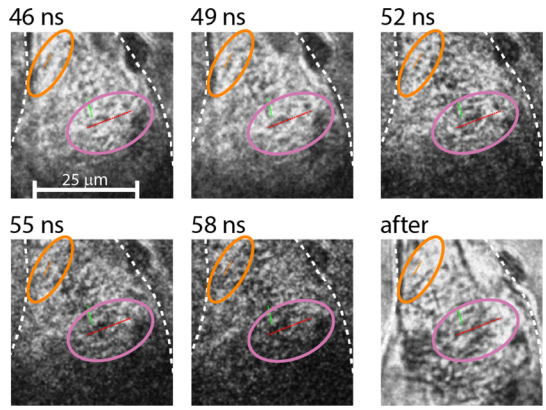

Figure 12. Zoomed-in view of deformations in the RDX crystal from Figures 10 and 11. The orange, red, and green dashed lines indicate locations in which planes evolve along the 0°, 59°, and −24° directions, respectively, over the course of the image progression.

The orange dashed line in Figure 12 (circled in orange) illustrates the motion that we observe for some deformation planes, which we detect as a gradual shift in the line over the course of the image sequence. While the dashed line is drawn over the same place in each frame, the deformation plane both moves and lengthens over the image sequence. Altogether, the deformation plane migrated ∼5 μm by the time the sample was recovered. In contrast, the green dashed line (drawn parallel and to the right of the initial deformation line) demonstrates deformation planes that remain essentially stationary. While this plane moved almost imperceptibly between each subsequent in situ frame, it shifted at longer times t > 58 ns.

The red dashed line in Figure 12 marks the position in each image where a very long feature eventually forms. Frames from 46 to 58 ns in Figure 12 reveal that nearby short lines form and migrate to agglomerate along the red line. As the lines coalesce, the shape of the feature distorts to accommodate the directions

https://dx.doi.org/10.1021/acs.jpca.9b07637
J. Phys. Chem. A 2020, 124, 3301−3313

of the short linear components, suggesting that differences among the directions of nearby lines do not preclude their interactions. Similar distortion and migration patterns are observable for other planes from the image progression in Figure 12.

The complicated evolution of the features as they grow—long after the shock has passed—suggests dynamics on some length scales that we cannot resolve in our images.[57] Low mobility along some planes suggests different deformation mechanisms along those directions (e.g., high mobility causes plasticity, while low mobility causes fracture[16]). Further detail about the origins of different behavior along different planes requires information about the crystallographic orientation of the crystal, which has not been resolved.

4. DISCUSSION

As has been described previously,[41,48] the waveguide geometry used herein supports shock waves with a constantly varying pressure. This means that a gradual release of the shock pressure begins immediately following the shock front, without a sustained region of constant high pressure (i.e., an unsustained shock). Previous interferometric measurements have determined that the duration of the elevated pressure for these shocks is ∼15−20 ns, with most of the duration corresponding to the gradual release of pressure.[48] To understand the RDX shock response in this waveguide system, we use the quantifiable results from the USAXS and photoemission measurements to interpret the deformation trends we observe from our image sequences.

The pressure-thresholded photoemission we observed in the cylindrically shocked RDX demonstrates that a shock with $P >$ 12 GPa is required to have sufficient energy to initiate the radiative response. In RDX, short-lived photoemission may result from either short-lived chemistry[20] or fracture.[58] During decomposition, photoemission is produced by spontaneous emission from electronically excited gas-phase molecules that are produced by the reactions.[59] In contrast, fractoluminescence (termed "triboluminescence under vacuum") originates from electrons that are liberated when the crystal cleaves upon reaching its yield stress.[58,60] As the emission we observe from our RDX crystals exceeds that of our control experiments over long timescales above 12 GPa, we hypothesize that the emission originates from chemistry over ∼50 ns timescales. Our USAXS data corroborate our hypothesis by quantifying the shapes and volume fractions in recovered crystals. While fractoluminescence would leave behind cleaved crystal surfaces (interfaces) with planar voids (cracks) in our recovered crystals, we only observed oblong voids (nearly planar) for crystals recovered from low-pressure (non-radiative) shocks. In contrast, crystals recovered from high-pressure shock waves produced a higher density of small spherical voids. We note that our RDX samples were single crystals, that is, not polycrystalline with multiple domains, but they were far from pristine. Growth defects such as solvent inclusions and others likely contributed to the development of hotspots.

The strong pressure threshold we observe in both USAXS and photoluminescence suggests a change in the mechanism by which the RDX responds to shocks with >12 GPa. The unresolved shapes in Figure 3 that appeared within ∼1 ns of the shock front suggest that the initial damage occurs under compression (i.e., during the 10−15 ns duration of the wave in this experimental geometry[48]). While further damage likely follows the shock front and pressure release (i.e., under tension[62] or subsequent spall[63] and afterward), the appearance of distinct features within ∼1 ns of the shock front demonstrates an initial response preceding rarefaction. From the timescales and void morphologies we observe, we hypothesize that low-pressure shocks ($P <$ 12 GPa) initiate non-radiative planar deformations (i.e., fracture or slip), while high-pressure shocks ($P >$ 12 GPa) initiate local chemical decomposition.[64,65]

We hypothesize that the correlated chemistry and very small spherical void structures are indicative of sub-critical hotspots formed by the shock. This model—first proposed by Yoffe[4]—predicts that the temperature and pressure behind the shock front localize around initial defects in an energetic material to initiate decomposition.[5,66,9] The heat produced from the initial reaction may then locally propagate the thermally activated chemistry. As the chemistry in RDX forms predominantly gas-phase products,[59] localized chemistry should create small voids with a shape that corresponds to that of the reacted zone. We therefore propose that the emission and void morphology indicate short-lived chemistry at small hotspots in the initial 50 ns following the $P >$ 12 GPa shock wave.

For $P <$ 12 GPa, we observe immobile deformation planes only along a single direction within the crystal. This suggests that in the absence of resolvable chemistry, low-pressure shocks reveal a single uniquely sensitive direction in the crystal even as the stress is applied by a multidirectional cylindrically converging shock wave. Above the ∼12 GPa threshold, we observe different families of deformation planes that appear as the chemiluminescence subsides ($t <$ 50 ns). The chemistry occurs near the time that the shock pressure traverses the RDX crystal, creating sub-micrometer-sized features in our optical images. Even beyond the timescale of the chemiluminescence, we observe deformations along multiple directions—after the crystal has been successively compressed and released twice and heated to an elevated shock temperature. As previous work has demonstrated that hotspots may be formed by dislocation pileup,[10] a detailed X-ray characterization is required to determine what types of defects and specific crystallographic axes are inherent to the "deformation planes" we observe optically. Given the relevant timescales for the optical deformation features, we hypothesize that the deformations may be caused either by a pileup of nanoscale deformations or by localized pressure from pockets of product gases trapped in the crystal.

We note that phase transitions to the γ or ε phases have been observed for shocks with $P >$ 4 GPa. All of our shock pressures in this work have exceeded 4 GPa, and our observed pressure threshold for chemical decomposition does not match the known phase-transition pressure. Considerations such as the kinetics of phase transitions and reversion to the original phase after pressure release, over-driving of phase transitions at high pressures,[60,61] and the variation of phase transition behavior as a function of shock propagation direction warrant further study and are beyond the scope of this work.

While additional detail is required to fully understand the detailed mechanisms of the changes we observed, our results show reproducible dynamics as RDX crystals embedded in a polymer binder respond to a non-planar shock wave. As shock reflections in application-relevant PBX composites are known to change the shock geometry,[11] detailed experiments are required to investigate how changes to the shock geometry influence the resulting chemistry. Uniaxial shocks along crystalline symmetry directions may be described by a single-

https://dx.doi.org/10.1021/acs.jpca.9b07637
J. Phys. Chem. A 2020, 124, 3301−3313

strain tensor component; however, converging waveguide shock waves include additional stress components that exert different stresses upon the RDX crystals. Inhomogeneity in the shock direction for converging shocks creates additional instability, making a direct comparison between uniaxial and waveguide converging shocks difficult.

Previous investigations have shown that uniaxial shocks induce fracture or deformation in RDX and HMX, with crystallographic planes that are activated depending on their orientation with respect to the shock direction.[15,24,25,27,67] This occurs because each slip system requires sufficient stresses to activate and cause fracture, slip, or shear banding, which requires the shock stress to have sufficient components along specific crystallographic directions. Our experimental geometry is more representative of the stresses exerted in real PBX formulations, in which small crystallites are randomly oriented and in contact with a polymer binder, leading to complex and turbulent shock geometries. The deformations we observed in RDX suggest that nonplanar shocks cause the crystals to deform first along well-defined sensitive plane before deforming along additional directions. Despite the complexity of the initial stresses, direct real-time imaging of how individual crystals respond to the shock collected with real-time emission and characterization of the void distributions in the recovered crystals has revealed a dominant preferential response in RDX crystals at moderate pressures.

5. CONCLUSIONS

This work demonstrated that converging shock waves in RDX produce plasticity and chemical activation that are strongly thresholded by the shock pressure. For low-pressure shocks with $P < 12$ GPa, we observe nonradiative shock responses that form roughly planar nanovoids that grow along a single direction. High-pressure shocks above 12 GPa result in photoemission from RDX decomposition products followed by the onset of plasticity or fracture along several families of deformation planes, with small spherical voids that are observed after recovery.

At all pressures, the directional specificity of deformation planes does not correlate to the directions of applied stress in the crystal, suggesting inherent lattice sensitivities in RDX. Above the pressure threshold to activate chemistry, we observe a cascade of deformations along up to seven different directions, with evolution and partial coalescence over tens of nanoseconds that further evolved after our real-time measurements before reaching the final recovered state. The timescale of the high-pressure deformation dynamics and photoemission suggests that the deformations may be driven by evolving forces within the crystal, including stresses arising from the formation of trapped gaseous reaction products. Our observations of the dynamic responses in RDX to cylindrical shock waves that exert stresses along many crystallographic directions provide new insight into the responses of randomly oriented crystals to geometrically distorted shock waves that occur in real-world PBX formulations.

■ ASSOCIATED CONTENT

Supporting Information

The Supporting Information is available free of charge at https://pubs.acs.org/doi/10.1021/acs.jpca.9b07637.

Additional experimental details for imaging and scattering experiments to detail how the analysis corroborates our interpretation and additional image sequences to display the trends in our data. (PDF)

■ AUTHOR INFORMATION

Corresponding Author

Leora E. Dresselhaus-Cooper − *Department of Chemistry and Institute for Soldier Nanotechnology, Massachusetts Institute of Technology, Cambridge, Massachusetts 02139, United States;* orcid.org/0000-0002-0757-0159; Email: dresselhausc1@llnl.gov

Authors

Dmitro J. Martynowych − *Department of Chemistry and Institute for Soldier Nanotechnology, Massachusetts Institute of Technology, Cambridge, Massachusetts 02139, United States;* orcid.org/0000-0001-6782-3675

Fan Zhang − *Materials Measurement Science Division, National Institute of Standards and Technology, Gaithersburg, Maryland 20899, United States;* orcid.org/0000-0003-1248-0278

Charlene Tsay − *Department of Chemistry, University of California Riverside, Riverside, California 92521, United States*

Jan Ilavsky − *X-ray Science Division, Argonne National Laboratory, Argonne, Illinois 60439, United States*

SuYin Grass Wang − *ChemMatCARS, Center for Advanced Radiation Sources, The University of Chicago, Argonne, Illinois 60439, United States;* orcid.org/0000-0001-8474-9817

Yu-Sheng Chen − *ChemMatCARS, Center for Advanced Radiation Sources, The University of Chicago, Argonne, Illinois 60439, United States*

Keith A. Nelson − *Department of Chemistry and Institute for Soldier Nanotechnology, Massachusetts Institute of Technology, Cambridge, Massachusetts 02139, United States*

Complete contact information is available at: https://pubs.acs.org/10.1021/acs.jpca.9b07637

Author Contributions

The project was directed by K.A.N. Shock experiments were carried out by L.E.D.-C. Samples were prepared by L.E.D.-C and D.M. USAXS experiments were performed by L.E.D.-C., F.Z., J.I., and D.M. The orientation of the crystal in Figure 7, was measured by L.E.D.-C., C.T., S.Y.G.W., and Y.-S.C. The analysis of the results was carried out by L.E.D.-C. and K.A.N. The paper was written by L.E.D.-C., with supporting contributions from all authors.

Notes

The authors declare no competing financial interest.

■ ACKNOWLEDGMENTS

The authors acknowledge William DiNatale, Peter Mueller, Charlie Settens, and Steven Kooi for their instruction and guidance in using MIT instrumentation facilities. The authors also acknowledge Jon Eggert, Betsy Rice, Brian Barnes, and Lara Leininger for their conversations that helped guide some of the analysis for this work. The work was supported by the Office of Naval Research grants N00014-16-1-2090 and (DURIP) N00014-15-1-2879. This research used resources of the Advanced Photon Source, a U.S. Department of Energy (DOE) Office of Science User Facility operated for the DOE Office of Science by Argonne National Laboratory under contract no. DE-AC02-06CH11357. NSF's ChemMatCARS Sector 15 was supported by the National Science Foundation under grant number NSF/CHE-1834750. While at LLNL,

L.E.D.-C.'s contributions to this article have been at Lawrence Livermore National Security, LLC under Contract No. DEAC52-07NA27344 with the U.S. Department of Energy, with support from the Lawrence Fellowship.

■ ADDITIONAL NOTE

[a]Certain commercial instruments, materials, or processes are identified in this paper to adequately specify the experimental procedure. Such identification does not imply recommendation or endorsement by the National Institute of Standards and Technology, nor does it imply that the instruments, materials, or processes identified are necessarily the best available for the purpose.

■ REFERENCES

(1) Dlott, D. D. Thinking Big (and Small) about Energetic Materials. *Mater. Sci. Technol.* **2006**, *22*, 463−473.
(2) Peiris, S. M.; Piermarini, G. J. *Static Compression of Energetic Materials*; Shock Wave and High Pressure Phenomena; Springer-Verlag: Heidelberg, 2008.
(3) Walley, S. M.; Field, J. E.; Greenaway, M. W. Crystal Sensitivities of Energetic Materials. *Mater. Sci. Technol.* **2006**, *22*, 402−413.
(4) Bowden, F. P.; Yoffe, A. Hot Spots and the Initiation of Explosion. *Symp. Combust. Flame Explos. Phenom.* **1948**, *3*, 551−560.
(5) Tarver, C. M.; Chidester, S. K.; Nichols, A. L., III Critical Conditions for Impact- and Shock-Induced Hot Spots in Solid Explosives. *J. Phys. Chem.* **1996**, *100*, 5794−5799.
(6) Dlott, D. D.; Fayer, M. D. Shocked Molecular Solids: Vibrational up Pumping, Defect Hot Spot Formation, and the Onset of Chemistry. *J. Chem. Phys.* **1990**, *92*, 3798.
(7) Tokmakoff, A.; Fayer, M. D.; Dlott, D. D. Chemical Reaction Initiation and Hot-Spot Formation in Shocked Energetic Molecular Materials. *J. Phys. Chem.* **1993**, *97*, 1901−1913.
(8) Field, J. E. Hot Spot Ignition Mechanisms for Explosives. *Acc. Chem. Res.* **1992**, *25*, 489−496.
(9) You, S.; Chen, M.; Dlott, D. D.; Suslick, K. S. Ultrasonic Hammer Produces Hot Spots in Solids. *Nat. Commun.* **2015**, *6*, 6581.
(10) Armstrong, R. W.; Ammon, H. L.; Elban, W. L.; Tsai, D. H. Investigation of Hot Spot Characteristics in Energetic Crystals. *Thermochim. Acta* **2002**, *384*, 303−313.
(11) An, Q.; Goddard, W. A., III; Zybin, S. V.; Jaramillo-Botero, A.; Zhou, T. Highly Shocked Polymer Bonded Explosives at a Nonplanar Interface: Hot-Spot Formation Leading to Detonation. *J. Phys. Chem. C* **2013**, *117*, 26551−26561.
(12) Strachan, A.; Kober, E. M.; van Duin, A. C. T.; Oxgaard, J.; Goddard, W. A., III Thermal Decomposition of RDX from Reactive Molecular Dynamics. *J. Chem. Phys.* **2005**, *122*, 054502.
(13) Stoltz, C. A.; Mason, B. P.; Hooper, J. Neutron Scattering Study of Internal Void Structure in RDX. *J. Appl. Phys.* **2010**, *107*, 103527.
(14) Doherty, R. M.; Watt, D. S. Relationship Between RDX Properties and Sensitivity. *Propellants, Explos., Pyrotech.* **2008**, *33*, 4−13.
(15) Cawkwell, M. J.; Ramos, K. J.; Hooks, D. E.; Sewell, T. D. Homogeneous Dislocation Nucleation in Cyclotrimethylene Trinitramine under Shock Loading. *J. Appl. Phys.* **2010**, *107*, 063512.
(16) Ramos, K. J.; Hooks, D. E.; Bahr, D. F. Direct Observation of Plasticity and Quantitative Hardness Measurements in Single Crystal Cyclotrimethylene Trinitramine by Nanoindentation. *Philos. Mag.* **2009**, *89*, 2381−2402.
(17) Dickinson, J. T.; Jensen, L. C.; Miles, M. H.; Yee, R. Fracto-Emission Accompanying Adhesive Failure between Rocket Propellent Constituents. *J. Appl. Phys.* **1987**, *62*, 2965−2971.
(18) LaBarbera, D. A.; Zikry, M. A. Dynamic Fracture and Local Failure Mechanisms in Heterogeneous RDX-Estane Energetic Aggregates. *J. Mater. Sci.* **2015**, *50*, 5549−5561.
(19) Dreger, Z. A.; McCluskey, M. D.; Gupta, Y. M. High Pressure-High Temperature Decomposition of γ-Cyclotrimethylene Trinitramine. *J. Phys. Chem. A* **2012**, *116*, 9680−9688.
(20) Patterson, J. E.; Dreger, Z. A.; Miao, M.; Gupta, Y. M. Shock Wave Induced Decomposition of RDX: Time-Resolved Spectroscopy. *J. Phys. Chem. A* **2008**, *112*, 7374−7382.
(21) Armstrong, R. W.; Coffey, C. S.; Devost, V. F.; Elban, W. L. Crystal Size Dependence for Impact Initiation of Cyclotrimethylene-trinitramine Explosive. *J. Appl. Phys.* **1990**, *68*, 979−984.
(22) Dlott, D. D. Ultrafast Spectroscopy of Shock Waves in Molecular Materials. *Annu. Rev. Phys. Chem.* **1999**, *50*, 251−278.
(23) Glenzer, S. H.; Fletcher, L. B.; Galtier, E.; Nagler, B.; Alonso-Mori, R.; Barbrel, B.; Brown, S. B.; Chapman, D. A.; Chen, Z.; Curry, C. B.; et al. Matter under Extreme Conditions Experiments at the Linac Coherent Light Source. *J. Phys. B* **2016**, *49*, 092001.
(24) Cawkwell, M. J.; Sewell, T. D.; Zheng, L.; Thompson, D. L. Shock-Induced Shear Bands in an Energetic Molecular Crystal: Application of Shock-Front Absorbing Boundary Conditions to Molecular Dynamics Simulations. *Phys. Rev. B: Condens. Matter Mater. Phys.* **2008**, *78*, 014107.
(25) An, Q.; Liu, Y.; Zybin, S. V.; Kim, H.; Goddard, W. A. Anisotropic Shock Sensitivity of Cyclotrimethylene Trinitramine (RDX) from Compress-and-Shear Reactive Dynamics. *J. Phys. Chem. C* **2012**, *116*, 10198−10206.
(26) De, S.; Zamiri, A. R.; Rahul. A Fully Anisotropic Single Crystal Model for High Strain Rate Loading Conditions with an Application to α-RDX. *J. Mech. Phys. Solids* **2014**, *64*, 287−301.
(27) Munday, L. B.; Solares, S. D.; Chung, P. W. Generalized Stacking Fault Energy Surfaces in the Molecular Crystal ARDX. *Philos. Mag.* **2012**, *92*, 3036−3050.
(28) Luscher, D. J.; Addessio, F. L.; Cawkwell, M. J.; Ramos, K. J. A Dislocation Density-Based Continuum Model of the Anisotropic Shock Response of Single Crystal α-Cyclotrimethylene Trinitramine. *J. Mech. Phys. Solids* **2017**, *98*, 63−86.
(29) Choi, C. S.; Prince, E. The Crystal Structure of Cyclotrimethylene-Trinitramine. *Acta Crystallogr., Sect. B: Struct. Crystallogr. Cryst. Chem.* **1972**, *28*, 2857−2862.
(30) Halfpenny, P. J.; Roberts, K. J.; Sherwood, J. N. Dislocations in Energetic Materials. Part 3. Etching and Microhardness Studies of Pentaerythritol Tetranitrate and Cyclotrimethylenetrinitramine. *J. Mater. Sci.* **1984**, *19*, 1629−1637.
(31) Elban, W. L.; Armstrong, R. W.; Yoo, K. C.; Rosemeier, R. G.; Yee, R. Y. X-Ray Reflection Topographic Study of Growth Defect and Microindentation Strain Fields in an RDX Explosive Crystal. *J. Mater. Sci.* **1989**, *24*, 1273−1280.
(32) Sandusky, H. W.; Beard, B. C.; Glancy, B. C.; Elban, W. L.; Armstrong, R. W. Comparison of Deformation and Shock Reactivity for Single Crystals of RDX and Ammonium Perchlorate. *MRS Proc.* **1992**, *296*, 93.
(33) Coffey, C. S.; Sharma, J. Lattice Softening and Failure in Severely Deformed Molecular Crystals. *J. Appl. Phys.* **2001**, *89*, 4797−4802.
(34) Sharma, J.; Armstrong, R. W.; Elban, W. L.; Coffey, C. S.; Sandusky, H. W. Nanofractography of Shocked RDX Explosive Crystals with Atomic Force Microscopy. *Appl. Phys. Lett.* **2001**, *78*, 457−459.
(35) Strachan, A.; van Duin, A.; Chakraborty, D.; Dasgupta, S.; Goddard, W. Shock Waves in High-Energy Materials: The Initial Chemical Events in Nitramine RDX. *Phys. Rev. Lett.* **2003**, *91*, 098301.
(36) Zhang, L.; Zybin, S. V.; Van Duin, A. C. T.; Goddard, W. A., III Modeling High Rate Impact Sensitivity of Perfect RDX and HMX Crystals by ReaxFF Reactive Dynamics. *J. Energ. Mater.* **2010**, *28*, 92−127.
(37) Radha, P. B.; Betti, R.; Boehly, T. R.; Delettrez, J. A.; Edgell, D. H.; Goncharov, V. N.; Igumenshchev, I. V.; Knauer, J. P.; Marozas, J. A.; Marshall, F. J.; et al. Inertial Confinement Fusion Using the OMEGA Laser System. *IEEE Trans. Plasma Sci.* **2011**, *39*, 1007−1014.

https://dx.doi.org/10.1021/acs.jpca.9b07637
J. Phys. Chem. A 2020, 124, 3301−3313

(38) Watanabe, M.; Takayama, K. Stability of Converging Cylindrical Shock Waves. *Shock Waves* **1991**, *1*, 149−160.
(39) An, Q.; Goddard, W. A., III; Zybin, S. V.; Luo, S.-N. Inhibition of Hotspot Formation in Polymer Bonded Explosives Using an Interface Matching Low Density Polymer Coating at the Polymer-Explosive Interface. *J. Phys. Chem. C* **2014**, *118*, 19918−19928.
(40) Pezeril, T.; Saini, G.; Veysset, D.; Kooi, S.; Fidkowski, P.; Radovitzky, R.; Nelson, K. A. Direct Visualization of Laser-Driven Focusing Shock Waves. *Phys. Rev. Lett.* **2011**, *106*, 214503.
(41) Dresselhaus-Cooper, L.; Gorfain, J. E.; Key, C. T.; Ofori-Okai, B. K.; Ali, S. J.; Martynowych, D. J.; Gleason, A.; Kooi, S.; Nelson, K. A. Development of Single-Shot Multi-Frame Imaging of Cylindrical Shock Waves in a Multi-Layered Assembly. *Sci. Rep.* **2019**, *9*, 3689.
(42) Howard, M.; Hock, M. C.; Meehan, B. T.; Dresselhaus-Cooper, L. E. A Locally Adapting Technique for Edge Detection Using Image Segmentation. *SIAM J. Sci. Comput.* **2018**, *40*, B1161−B1179.
(43) Dresselhaus-Cooper, L.; Howard, M.; Hock, M. C.; Meehan, B. T.; Ramos, K. J.; Bolme, C. A.; Sandberg, R. L.; Nelson, K. A. Machine Learning to Analyze Images of Shocked Materials for Precise and Accurate Measurements. *J. Appl. Phys.* **2017**, *122*, 104902.
(44) Forbes, J. W. Impedance Matching Techniques. In *Shock Wave Compression of Condensed Matter*; Springer-Verlag: Berlin Hiedelberg, 2012; p 374.
(45) Chester, W. CXLV. The quasi-cylindrical shock tube. *London Edinburgh Philos. Mag. J. Sci.* **1954**, *45*, 1293−1301.
(46) Chisnell, R. F. The Normal Motion of a Shock Wave through a Non-Uniform One-Dimensional Medium. *Proc. R. Soc. London, Ser. A* **1955**, *232*, 350−370.
(47) Whitham, G. B. New Approach to Problems of Shock Dynamics Part I. Two-Dimensional Problems. *J. Fluid Mech.* **1957**, *2*, 145−171.
(48) Veysset, D.; Maznev, A.; Pezeril, T.; Kooi, S. E.; Nelson, K. A. Interferometric Analysis of Laser-Driven Cylindrically Focusing Shock Waves in a Thin Liquid Layer. *Sci. Rep.* **2016**, *6*, 24.
(49) Maharrey, S.; Behrens, R. Thermal Decomposition of Energetic Materials. 5. Reaction Processes of 1,3,5-Trinitrohexahydro-s-Triazine below Its Melting Point. *J. Phys. Chem. A* **2005**, *109*, 11236−11249.
(50) Ilavsky, J.; Zhang, F.; Andrews, R. N.; Kuzmenko, I.; Jemian, P. R.; Levine, L. E.; Allen, A. J. Development of Combined Microstructure and Structure Characterization Facility for in Situ and Operando Studies at the Advanced Photon Source. *J. Appl. Crystallogr.* **2018**, *51*, 867−882.
(51) Ilavsky, J.; Jemian, P. R. Irena: Tool Suite for Modeling and Analysis of Small-Angle Scattering. *J. Appl. Crystallogr.* **2009**, *42*, 347−353.
(52) Zhang, F.; Levine, L. E.; Allen, A. J.; Stoudt, M. R.; Lindwall, G.; Lass, E. A.; Williams, M. E.; Idell, Y.; Campbell, C. E. Effect of Heat Treatment on the Microstructural Evolution of a Nickel-Based Superalloy Additive-Manufactured by Laser Powder Bed Fusion. *Acta Mater.* **2018**, *152*, 200−214.
(53) Wiederhorn, S. M.; Johnson, H.; Diness, A. M.; Heuer, A. H. Fracture of Glass in Vacuum. *J. Am. Ceram. Soc.* **1974**, *57*, 336−341.
(54) Taguchi, K.; Miyaji, H.; Izumi, K.; Hoshino, A.; Miyamoto, Y.; Kokawa, R. Growth Shape of Isotactic Polystyrene Crystals in Thin Films. *Polymer* **2001**, *42*, 7443−7447.
(55) Ben-Dor, G. *Shock Wave Reflection Reflection Phenomena*, 2nd ed.; Davison, L., Horie, Y., Eds.; Shock Wave and High Pressure Phenomena; Springer-Verlag: Berlin Heidelberg New York, 2007.
(56) Armstrong, R. W. Dislocation Mechanics Aspects of Energetic Material Composites. *Rev. Adv. Mater. Sci.* **2009**, *19*, 13−40.
(57) Bulatov, V. V.; Hsiung, L. L.; Tang, M.; Arsenlis, A.; Bartelt, M. C.; Cai, W.; Florando, J. N.; Hiratani, M.; Rhee, M.; Hommes, G.; et al. Dislocation Multi-Junctions and Strain Hardening. *Nature* **2006**, *440*, 1174−1178.
(58) Dickinson, J. T.; Miles, M. H.; Elban, W. L.; Rosemeier, R. G. Fractoemission from Cyclotrimethylenetrinitramine (RDX) Explosive Single Crystals. *J. Appl. Phys.* **1984**, *55*, 3994−3998.
(59) Miao, M.; Dreger, Z. A.; Patterson, J. E.; Gupta, Y. M. Shock Wave Induced Decomposition of RDX: Quantum Chemistry Calculations. *J. Phys. Chem. A* **2008**, *112*, 7383−7390.
(60) Tsuboi, Y.; Seto, T.; Kitamura, N. Laser-Induced Shock Wave Can Spark Triboluminescence of Amorphous Sugars. *J. Phys. Chem. A* **2008**, *112*, 6517−6521.
(61) Halfpenny, P. J.; Roberts, K. J.; Sherwood, J. N. Dislocations in Energetic Materials. IV. The Crystal Growth and Perfection of Cyclotrimethylene Trinitramine (RDX). *J. Cryst. Growth* **1984**, *69*, 73−81.
(62) Belak, J. On the Nucleation and Growth of Voids at High Strain-Rates. *J. Comput.-Aided Mater. Des.* **1998**, *5*, 193−206.
(63) Li, W. H.; Yao, X. H. The Spallation of Single Crystal SiC: The Effects of Shock Pulse Duration. *Comput. Mater. Sci.* **2016**, *124*, 151−159.
(64) Germann, T. C.; Holian, B. L.; Lomdahl, P. S.; Tanguy, D.; Mareschal, M.; Ravelo, R. Dislocation Structure behind a Shock Front in FCC Perfect Crystals: Atomistic Simulation Results. *Metall. Mater. Trans. A* **2004**, *35*, 2609−2615.
(65) Zybin, S. V.; Elert, M. L.; White, C. T. Nanoscale View of Shock-Wave Splitting in Diamond. *Metall. Mater. Trans. A* **2004**, *35*, 2647−2650.
(66) Hooper, J. Vibrational Energy Transfer in Shocked Molecular Crystals. *J. Chem. Phys.* **2010**, *132*, 014507.
(67) Grilli, N.; Duarte, C. A.; Koslowski, M. Dynamic Fracture and Hot-Spot Modeling in Energetic Composites. *J. Appl. Phys.* **2018**, *123*, 065101.

https://dx.doi.org/10.1021/acs.jpca.9b07637
J. Phys. Chem. A 2020, 124, 3301−3313